JACS
JOURNAL OF THE AMERICAN CHEMICAL SOCIETY
Article
pubs.acs.org/JACS

Organometallic Complexes Anchored to Conductive Carbon for Electrocatalytic Oxidation of Methane at Low Temperature

Madhura Joglekar,[†,⊥] Vinh Nguyen,[‡,⊥] Svitlana Pylypenko,[†] Chilan Ngo,[†] Quanning Li,[‡] Matthew E. O'Reilly,[§] Tristan S. Gray,[§] William A. Hubbard,[∥] T. Brent Gunnoe,[*,§] Andrew M. Herring,[*,‡] and Brian G. Trewyn[*,†]

[†]Department of Chemistry and Geochemistry, Colorado School of Mines, Golden, Colorado 80401, United States
[‡]Department of Chemical and Biological Engineering, Colorado School of Mines, Golden, Colorado 80401, United States
[§]Department of Chemistry, University of Virginia, Charlottesville, Virginia 22904, United States
[∥]Department of Physics, University of California—Los Angeles, Los Angeles, California 90095, United States

Ⓢ *Supporting Information*

ABSTRACT: Low-temperature direct methane fuel cells (DMEFCs) offer the opportunity to substantially improve the efficiency of energy production from natural gas. This study focuses on the development of well-defined platinum organometallic complexes covalently anchored to ordered mesoporous carbon (OMC) for electrochemical oxidation of methane in a proton exchange membrane fuel cell at 80 °C. A maximum normalized power of 403 μW/mg Pt was obtained, which was 5 times higher than the power obtained from a modern commercial catalyst and 2 orders of magnitude greater than that from a Pt black catalyst. The observed differences in catalytic activities for oxidation of methane are linked to the chemistry of the tethered catalysts, determined by X-ray photoelectron spectroscopy. The chemistry/activity relationships demonstrate a tangible path for the design of electrocatalytic systems for C−H bond activation that afford superior performance in DMEFC for potential commercial applications.

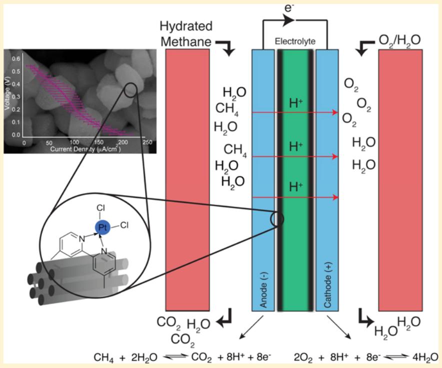

INTRODUCTION

Methane, a primary constituent of natural gas, has attracted widespread attention as a fuel due to its higher energy content per mass unit (55.7 kJ g^{-1}) compared to other hydrocarbons. In the past decade, advances in drilling technologies have expanded the access and reduced the expense of natural gas.[1] Currently, the predominant use of methane in the energy sector is via combustion. An alternative approach is to utilize methane in fuel cells. Fuel cells are dramatically more efficient than heat engines at lower temperatures and their exhaust is composed of only CO_2 and water making them attractive clean energy conversion devices. With the use of current technology, methane has been directly electrochemically oxidized only in solid oxide fuel cells (SOFCs) with most research focused on the development of new anode materials for this conversion.[2−6] However, the high operating temperatures (650−1100 °C) and substantial capital expenses for SOFCs keep this technology from being cost-effective and necessitates the need to develop alternatives.

Proton exchange membrane fuel cells (PEMFCs) have the advantage of much higher power densities, faster start up and shut down, good cyclability, and the potential for scalability from micro to large-scale distributed power generation; however, their lower temperature of operation makes the activation of methane extremely challenging under the operating conditions of the fuel cell. In 1962, Niedrach made the first attempt to demonstrate a DMEFC.[7] In 2012, Ferrell et al. reported methane activation using commercially available Pt ELAT and Pt−Ru ELAT gas-diffusion anode electrodes in a PEMFC.[8] However, negligible current densities were achieved in both studies, and in general, the cell could not be stabilized. Considering the very high C−H bond dissociation energy (435 kJ mol^{-1}) for methane, one of the major challenges is the development of catalysts that provide sufficient rates of C−H activation at the operating temperatures of PEMFC (60−100 °C). Despite the fact that some molecular transition complexes have been demonstrated to activate methane C−H bonds in homogeneous environments at temperatures more relevant for PEMFCs (≤200 °C),[9−18] to our knowledge there have been no attempts to incorporate these molecular systems into electrochemical environments for hydrocarbon oxidation in fuel cells.

Joglekar et al. have recently demonstrated a method to covalently anchor molecular complexes onto a conductive mesoporous carbon support.[19] This has been achieved through a lithiation strategy to selectively deprotonate defect sites in the graphitic structure of mesoporous carbons, thereby allowing covalent functionalization of the surface at the defect sites. A limited number of reports have indicated the use of molecular complexes adsorbed onto carbon surface as efficient catalysts for the oxygen reduction reaction (ORR) in methanol or hydrogen PEMFCs.[20,21]

Received: June 19, 2015

DOI: 10.1021/jacs.5b06392

Recently, an ethanol fuel cell was developed using Rh-based organometallic complexes adsorbed onto conductive Vulcan support, which generated electric power from the oxidation of ethanol to the acetate product.[22,23] These types of systems, wherein the molecular catalysts are adsorbed on the surface of carbon through noncovalent interactions, tend to fail in more complicated C−H activation systems, such as DMEFCs, due to the weak interactive forces between the molecular catalyst and the conductive carbon support. To address this, we have developed a new selective surface functionalization strategy for covalently tethering molecular complexes on the surface of ordered mesoporous carbon (OMC) materials. This enables us to introduce unique molecular systems into the fuel cell configurations. Previously, such materials were difficult to prepare due to the limitations of carbon functionalization techniques. The new OMC-support Pt catalysts afford the direct oxidation of methane without poisoning by carbon monoxide adsorption at low temperatures (<150 °C), leading to the design, fabrication and testing of new low temperature DMEFCs.

In contrast to the current technology for the direct conversion of methane using SOFCs that operate exclusively at very high temperatures (650−1100 °C), we report the first successful demonstration of electrooxidation of methane at 80 °C utilizing these novel OMC-bound C−H activating molecular catalysts.

■ EXPERIMENTAL SECTION

Synthesis of Large Pore Mesoporous Silica Nanoparticles (*l*-MSN). *l*-MSN template was synthesized according to a previously reported literature procedure.[24] A nonionic surfactant Pluronic P104 (7.0 g, BASF) was added to 1.6 M HCl (273.0 g) in a 500 mL Erlenmeyer flask. After the mixture stirred at 55 °C for 1 h, tetramethylorthosilicate (TMOS, 10.64 g, Sigma) was added at once and the reaction mixture was further stirred at 55 °C for 24 h. It is crucial to maintain a constant reaction temperature for 24 h in order to obtain *l*-MSN with uniform morphology and pore size. The mixture was then hydrothermally treated at 150 °C for 24 h in a Teflon lined autoclave. In the final step, the mixture was cooled, filtered, and washed with water and copious amounts of methanol to obtain a white powder. It was then lyophilized overnight, followed by calcination at 550 °C for 6 h at a ramp rate of 1.5 °C min^{-1} to remove the nonionic surfactant P104.

Synthesis of Ordered Mesoporous Carbon (OMC). OMC with uniform morphology was synthesized according to our recently published report.[19] Typically, 1 g of *l*-MSN having a pore volume of 1.12 $\text{cm}^3\ \text{g}^{-1}$ was impregnated with 1.20 g of sucrose and 7 g of water in a centrifuge tube and sonicated until all the particles were evenly dispersed. After this solution was transferred to a crucible, 0.13 g of concentrated sulfuric acid was added. The mixture was stirred to break any large chunks of *l*-MSN or sucrose and then heated at 100 and 160 °C for 6 h each. This process of addition and partial carbonization of sucrose, water, and concentrated sulfuric acid was repeated until the pore volume of the *l*-MSN template was reduced to approximately zero. The pore volume of the silica−carbon composite was determined after each step using the nitrogen sorption analysis. Also, the amounts of sucrose and sulfuric acid required for each step were determined based on the pore volume of the silica−carbon composite. The complete pyrolysis of carbon was carried out under nitrogen atmosphere at 900 °C for 5 h in a tube furnace. In the final step, the *l*-MSN template was etched with 10% HF overnight in centrifuge tubes. The resulting OMC was washed with copious amounts of water until the pH was neutral.

Covalent Attachment of Bipyridine or Phenanthroline to the Surface of OMC. All the reactions were performed under inert atmosphere using standard Schlenk line techniques. For the covalent attachment of 2,2′-bipyridine, the surface of OMC was first lithiated using *n*-butyllithium. In a typical procedure, a Schlenk flask was charged with 0.25 g of OMC and dried overnight under vacuum at 100 °C to remove all the moisture. The OMC was then suspended in 25 mL of diethyl ether and sonicated for 15 min to disperse the particles and break the larger aggregates. The mixture was kept under vigorous stirring and 2.5 mL of *n*-butyllithium (2.5 M in hexane, Sigma) was added dropwise at −78 °C. Following the addition, the mixture was stirred at room temperature for 4 h. In the meantime, 1.06 mmol of 6-bromo-2,2′-bipyridine purchased from Sigma was dried under vacuum. After 4 h, it was added to the Schlenk flask, and the mixture was further stirred for 2 h at 35 °C. To obtain surface functionalized OMC powder, the mixture was centrifuged and the supernatant was removed. During this step and all the further steps, no efforts were taken to exclude air. The product was washed with methanol 5 times and subsequently centrifuged. Finally, it was suspended in methanol overnight to remove any unreacted bipyridine and Li impurities from the pores and surface of OMC. It was then centrifuged and dried at 100 °C for 4 h. This product was termed as OMC-6Bp. For the synthesis of OMC-4Bp and OMC-phen, 1.06 mmol of 4,4′-dibromo-2,2′-bipyridine (purchased from Carbosynth) and 5-bromo-1,10-phenanthroline synthesized via a previously reported procedure[25] were vacuum-dried and added after 4 h following the addition of *n*-butyllithium in the above procedure.

Synthesis of $[\text{PtPh}_2(\mu\text{-SEt}_2)]_2$. The Pt dimeric complex was synthesized using a modification of a previously reported procedure.[26] In brief, 440 mg of commercially available yellow crystalline *cis*-$\text{PtCl}_2(\mu\text{-SEt}_2)_2$ was dispersed in 10 mL of diethyl ether in a Schlenk flask. The synthesis was done under inert atmosphere using standard Schlenk line techniques. To the above suspension, 4 mL of phenyl lithium solution (1.8 M in dibutylether, Sigma) was added dropwise over a course of 20 min at −78 °C. This suspension was allowed to stir for 2 h at 0 °C. After 2 h, 8 mL of distilled water was added dropwise over a course of 10 min under a constant nitrogen flow. A thick and nonsettling suspension was formed, which was filtered through 545 Celite. At this and all the subsequent points, no efforts were made to exclude air. The filtrate was poured into a separatory funnel and dichloromethane was added to it. The dichloromethane layer was washed three times with water, dried with magnesium sulfate, filtered through activated charcoal, and reduced to dryness to obtain a white solid. This was dissolved in 15 mL of dichloromethane and gently heated (40 °C) to ensure complete dissolution of the white solid. The mixture was filtered through a medium porosity frit into a flask, and the filtrate was concentrated to approximately 6 mL *in vacuo*. A white crystalline solid precipitated, which was dissolved in 50 mL of pentane. The crystallization was left at −20 °C overnight. White crystalline solid (75% yield) was obtained following filtration.

Synthesis of OMC-4Bp-Pt-Ph_2, OMC-6Bp-Pt-Ph_2, and OMC-phen-Pt-Ph_2. Platinum was coordinated to the bipyridyl ligand on the surface of OMC using the following procedure. OMC-4Bp, OMC-6Bp, or OMC-phen (0.1 g) and 0.03 mmol Pt-dimer were added in a Schlenk flask in anhydrous diethyl ether as a solvent. The reaction mixture was stirred at room temperature for 24 h under argon. Finally, the product was centrifuged and the supernatant was discarded. It was washed six times with ether to remove any unreacted, excess Pt-dimer and lyophilized overnight.

Synthesis of OMC-4Bp-Pt-Cl_2, OMC-6Bp-Pt-Cl_2, and OMC-phen-Pt-Cl_2. The chloro versions of the molecular complexes were synthesized using a procedure similar to the synthesis of homogeneous complexes and is as follows.[27] OMC-4Bp, OMC-6Bp, or OMC-phen (0.1 g) was added to a round-bottom flask containing 250 mL of distilled water and 0.2 mL of concentrated hydrochloric acid. A platinum precursor, K_2PtCl_4 (100 mg), was added to the same flask, and the reaction mixture was heated to reflux for 24 h. Finally, the powder was centrifuged, washed with copious amounts of distilled water, and lyophilized overnight.

Characterization. Small-angle X-ray scattering (SAXS) data was collected using a Rigaku S-Max 3000 High Brilliance three-pinhole SAXS system outfitted with a MicroMax-007HFM rotating anode (Cu Kα), Confocal Max-Flux Optic, Gabriel multiwire area detector, and a Linkam thermal stage. Exposure times for samples were typically on the order of 1200 s. Nitrogen sorption analyses were done on a Micromeritics Tristar 3000 surface area and porosity analyzer using Brunauer−Emmett−Teller (BET) equation to calculate the surface area and pore volume and the Barrett−Joyner−Halenda (BJH) method to calculate pore size distribution. Raman spectroscopy was done using

WITEC Alpha 300 confocal microscope. The morphology of the samples was analyzed using JEOL JSM-7000F field emission scanning electron microscope (FESEM). The samples were dispersed on a conductive carbon tape and analyzed using an accelerating voltage of 7 kV. High-resolution micrographs and X-ray energy dispersive spectroscopy (EDS) spot analysis were obtained using Philips CM200 transmission electron microscope operated at 200 kV and FEI Titan S/TEM operated at 300 kV. The samples were dispersed in 2 mL of ethanol and drop-casted onto lacey carbon TEM grids for observation. Thermogravimetric analysis was done in a SETSYS Evo system with B-type DTA measurement head and a temperature ramp rate of 10 °C min^{-1} in air for quantification of metal. Helium gas was used to maintain inert atmosphere in order to study the decomposition behavior of the tethered catalyst. XPS analysis was performed on a Kratos Nova X-ray photoelectron spectrometer equipped with a monochromatic Al Kα source operating at 300 W. Survey and high-resolution C 1s, O 1s, N 1s, Si 2p, Cl 2p, and Pt 4f spectra were acquired at 160 and 20 eV, respectively, providing charge compensation using low energy electrons. Three areas per sample were analyzed. Data analysis was performed using CasaXPS software. A linear background was applied to C 1s, O 1s, N 1s, Si 2p, and Cl 2p regions, and a Shirley background was applied to Pt 4f region. Quantification was performed using sensitivity factors supplied by manufacturer. Analysis included charge referencing to the internal aromatic carbon signal at 284.4 eV.

Materials for Methane Fuel Cell Testing. Methane cylinder purchased from General Air Corporation was used as received. Nafion-1110 membranes purchased from Ion Power were first cleaned and protonated by refluxing in 3% H_2O_2 for 1 h, followed by 1 h refluxing in DI water, 1 h refluxing in 0.5 N H_2SO_4, and finally 1 h refluxing in DI water. After conditionings, the membranes were stored in DI water at room temperature in the dark before use. The anode was fabricated with six different molecular catalysts prepared in our lab as previously described coating onto hydrophobic gas diffusion layers GDL LT 1400-W carbon cloth (E-tek). Detailed fabrication is illustrated in the following Membrane Electrode Assembly (MEA) Fabrication section. For the cathode, all fuel cells used Electrode Los Alamos Type (ELAT) prepared with ELAT LT 1400 gas diffusion layers (Nuvant Systems, Inc.) and containing 0.5 mg Pt/cm^2 (20% Pt on Vulcan XC-72 carbon). The 3M perfluorosulfonic acid ionomer with EW = 733 (structure given in the Supporting Information) as an aqueous dispersion was used in the catalyst layer.[28]

Membrane Electrode Assembly (MEA) Fabrication. Catalyst inks were first prepared as previously described by combining the desired catalyst, water, 2-propanol, and 3M ionomer dispersion.[8] The ionomer dispersion was added such that the 3M solid was 25% of the total mass of the catalyst and 3M solid in the ink. Water was added in an amount that was 10 times the mass of the catalyst in the ink. 2-Propanol was finally added in the ink to make water/2-propanol (3:2). The inks were sonicated in an ultrasonic bath for 5 min, followed by mixing with Vortex Mixer for 2 min. The sonicating and mixing process was repeated three times. The inks were finally airbrushed onto GDLs to make gas diffusion electrodes. Following airbrushing, the electrodes were placed under an IR 250W heat lamp to evaporate the water/2-propanol solvent in the catalyst layer. Both anode and cathode were prepared with an area of 5.48 cm^2. The electrodes were hot pressed on cleaned Nafion-1110 membranes using a digital combo multipurpose press, DC14 (GEO Knight & Co., Inc.), at 80 °C and 60 psig for 90 s. There was a small variation in the platinum loading on the anode ranging from 0.055 to 0.073 mg cm^{-2}, assuming homogeneous distribution. The loading of Pt on OMC for various complexes was in the range of 1.5−2.1 wt %.

Fuel Cell Testing. A single-cell hardware with an area of 5.48 cm^2 and single serpentine flow fields (Fuel Cell Technologies, Inc.) was used for this study. Humidified methane and oxygen were fed to the anode and cathode, respectively, at the same flow rate of 0.3 L/min. Both gases were flowed and humidified through sparging bottles with modular gas handling and gas metering system (Lynntech Industry, Inc.). Methane and oxygen were humidified at 60 and 80 °C, respectively. The cell, however, was maintained at 80 °C. The effluent from the fuel cell sweeps through the backpressure regulators and condenses liquid water in trap bottles. For this study, the backpressure was always kept at 30 psig during all fuel cells testing. The anode exit gas line was also connected with a CO_2 trap that contained 1 M NaOH solution. At the end of the testing procedure, the bicarbonate solution collected from this trap was analyzed by ^{13}C NMR spectroscopy to probe for the formation of CO_2. To test consistency and reproducibility of the MEA, each experiment was done in triplicate and demonstrated consistent results.

A Gamry Instruments potentiostat was used to perform polarization and electrochemical impedance spectroscopy (EIS) experiments as previously reported.[29] The polarization curves were obtained by first remaining at open circuit for 20 min. The potential was then stepped down from the open circuit potential until the limiting current was reached. For anode polarization, nitrogen instead of oxygen was fed to the cathode, which became a pseudoreference electrode. The potential was then scanned from open circuit to more positive potentials until a limiting current was achieved.

Measurement of Electrical Conductivity of the OMC Support and the OMC Bound Catalyst. A standard procedure was used to measure the bulk electrical conductivity of the OMC.[30] The results showed a decrease in the conductivity of OMC from 3.96 to 0.609 S cm^{-1} after functionalization measured at 127 psig. To boost the electrical conductivity of the catalyst, we added 20 wt % unfunctionalized OMC in with the OMC-4Bp-Pt-Cl_2 which had the highest catalytic activity. Our measured conductivity of 80 wt% OMC-4Bp-Pt-Cl_2 and 20 wt % OMC was 2.14 S cm^{-1}, demonstrating a clear improvement in conductivity by mixing functionalized and unfunctionalized OMC.

■ RESULTS AND DISCUSSION

Synthesis and Characterization of OMC-Tethered Single-Site Catalysts. Pt(II) complexes with chelating bis-nitrogen ligands have been studied for C−H activation of hydrocarbons, including alkanes.[13,14,31−33] The use of $[(\mathrm{bpy})\mathrm{Pt(Ph)(THF)}]^+$ (bpy = various 2,2′-bipyridyl ligands) and closely related complexes has been recently reported to catalyze the functionalization of benzene,[34−36] which has a C−H bond dissociation energy that is ∼29.3 kJ/mol stronger than that of methane. The demonstrated ability of these Pt(II) complexes to activate C−H bonds combined with the availability (both commercially and synthetically) of a variety of substituted 2,2′-bipyridyl compounds motivated us to start with (bpy)PtX_2 (X = Cl, phenyl) complexes as the molecular component for the new OMC-supported catalyst. OMCs have attracted significant attention as a conductive support for application in fuel cells due to their unique properties such as high surface area, uniform pore size distribution, interconnected mesopores and high conductivity.[37−39] In this study, a high surface area OMC support, used for anchoring the platinum-based catalysts, was prepared according to our recent report using large pore mesoporous silica nanoparticles (*l*-MSN) as a hard template.[19] As previously noted, this OMC support has a number of structural defect sites that can be leveraged for covalently anchoring catalysts on its surface. Accordingly, the defect sites on the surface of OMCs were initially deprotonated using a strong base, *n*-butyllithium, followed by the addition of a brominated ligand as shown in Figure 1.[19,40] This product was isolated, washed, lyophilized overnight and then coordinated with a platinum precursor such as K_2PtCl_4 or $[\mathrm{PtPh}_2(\mu\text{-SEt}_2)]_2$ to give the corresponding chlorine or phenyl versions of the molecular complexes (Figure 1). The OMC support and all the as-synthesized OMC-based catalysts were characterized using a range of spectroscopy and microscopy techniques. As seen in Figure S1 (Supporting Information), the nitrogen sorption isotherms of *l*-MSN, OMC and the OMC with covalently attached Pt indicate a type IV isotherm characteristic of mesoporous nanomaterials.[41] The pore size distribution is narrow for both the unfunctionalized OMC support and the surface

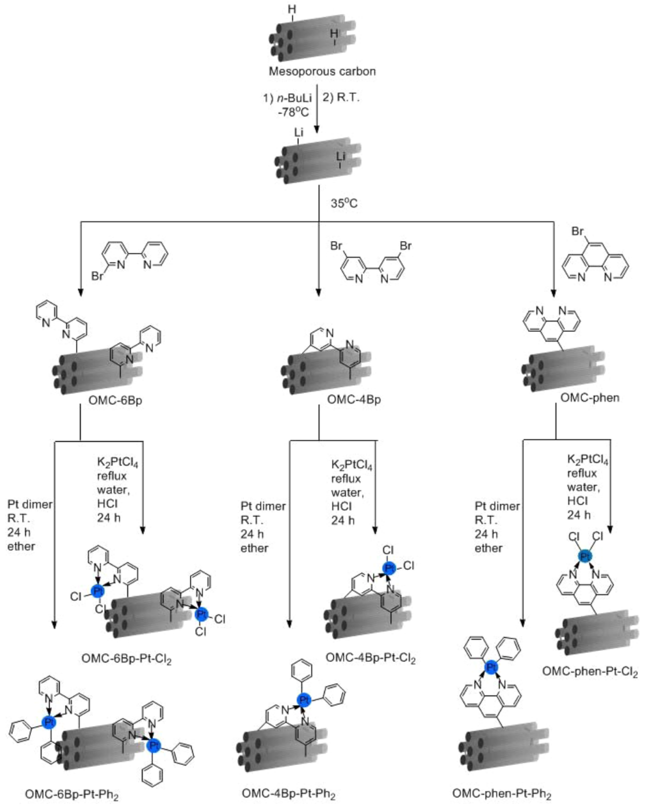

Figure 1. Schematic representation of the general synthetic procedure for OMC-tethered single-site catalysts.

modified ligand anchored OMC. Small angle X-ray scattering (SAXS) measurements were obtained to determine the pore arrangement of the original hard template and the synthesized OMC support. The *l*-MSN hard template has a 2D hexagonal arrangement of pores indicated by the 100, 110, and 200 peaks (Figure S2, Supporting Information), while the as-synthesized OMC support has a disordered arrangement of pores along the 110 and 200 planes as indicated by the absence of peaks (Figure S2, Supporting Information). The OMC particles are discrete with uniform morphology as indicated by the high-resolution transmission and scanning electron micrographs (Figure 2). The pore channels and the structure are also clearly visible in these micrographs (Figure 2D). High resolution scanning transmission electron micrographs (STEM) of the catalyst sample (Figures 2D and S14) OMC-4Bp-Pt-Cl_2 indicated negligible Pt nanoparticles on the OMC surface. Hence, the catalytic activity can be attributed to the tethered Pt (II) complex. EDX analysis revealed that C, O, N and Si were the major components (Figures S13 and S15, Supporting Information) in the catalyst samples. The Si content was attributed to the remnants of the silica template, in the amount less than 0.25 wt %. A small change in the I_D/I_G ratio (0.96 for OMC to 1.06 for OMC-4Bp-Pt-Cl_2) in the Raman analysis of the OMC-4Bp-Pt-Cl_2 sample revealed that the OMC structure was retained even after chemical modification of the surface (Figure S3c, Supporting Information). This observation was also consistent for the other OMC-based samples modified with bipyridine ligands tethered at the 6-position and phenanthroline ligands (Figure S3, Supporting Information).

Application of OMC-Tethered Single-Site Catalysts in DMEFC. Despite good gravimetric energy density (55.6 MJ kg^{-1}), the volumetric energy density of methane is very low (0.0378 MJ L^{-1}) and difficult to utilize at 1 bar since the fuel is not easily compressed. In addition, the electrooxidation of methane in acidic environments at low temperature remains exceedingly challenging.[8] A fuel cell running on methane requires water as an additional reactant at the anode (Figure 3A) and produces CO_2 at the anode as an oxidation product.

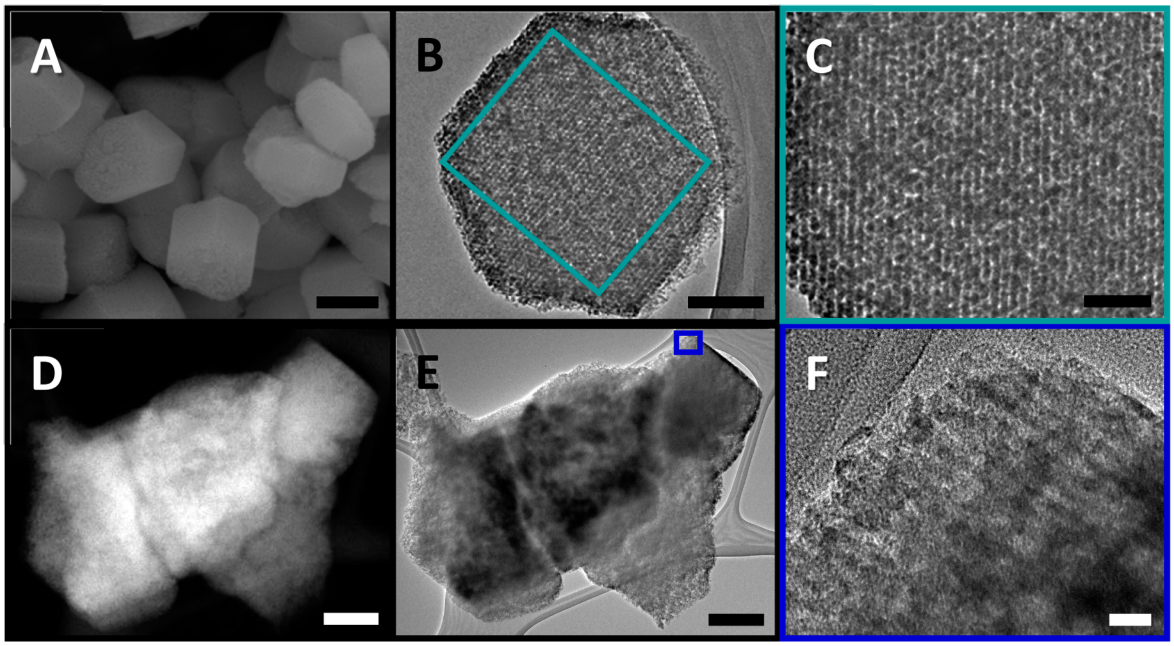

Figure 2. Characterization of the as-synthesized OMC support and the tethered molecular catalyst using electron microscopy. (A) Scanning electron micrograph of *l*-MSN hard template particles. Scale bar = 500 nm. (B and C) Transmission electron micrographs of a single OMC particle revealing the pore structure. Scale bars = 100 and 50 nm, respectively. (D) Scanning transmission electron micrograph of several overlapping OMC-4Bp-Pt-Cl_2 particles. Scale bar = 200 nm. (E) Bright-field TEM image corresponding to the STEM image in (D). Scale bar = 200 nm. (F) Higher magnification image of a thinner area on the edge of one particle, indicated by the blue box in (D) and showing the pore structure viewed from the side. Scale bar = 20 nm.

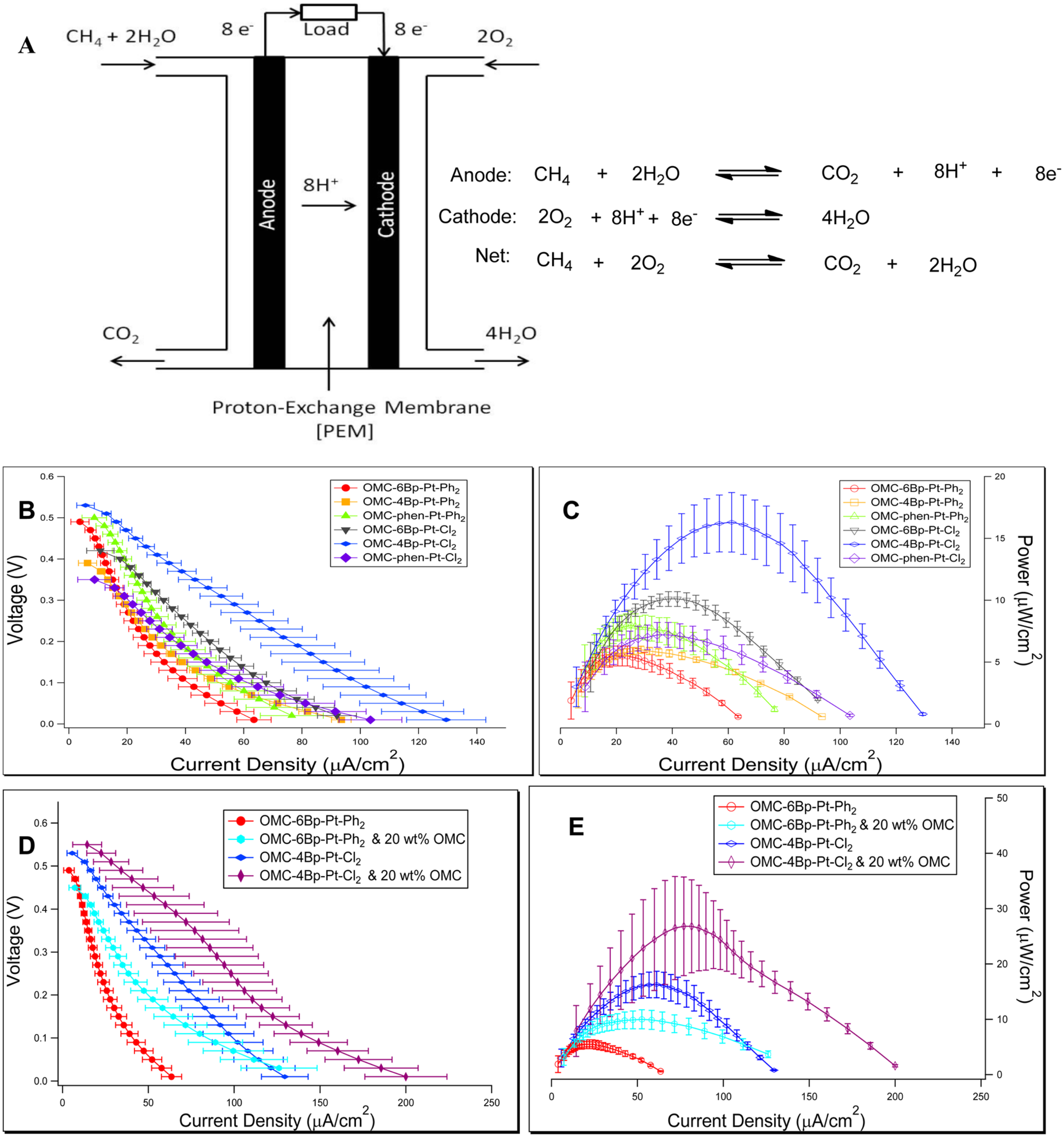

Figure 3. Polarization curves with power density performance of fuel cells with different molecular catalysts on the anode and the same commercial GDE containing 0.5 mg Pt cm^{-2} on the cathode. (A) Schematic representation and equation of the direct methane PEM fuel cell. (B) *V*−*I* curves of all catalysts tested in DMEFC. (C) *P*−*I* curves of all catalysts tested in DMEFC. (D) *V*−*I* curves of OMC-6Bp-Pt-Ph_2 (light blue and red) and OMC-4Bp-Pt-Cl_2 (dark blue and purple) on the anode before and after adding 20 wt % OMC. (E) *P*−*I* curves of OMC-6Bp-Pt-Ph_2 (light blue and red) and OMC-4Bp-Pt-Cl_2 (dark blue and purple) on the anode before and after adding 20 wt % OMC.

For the first time, using a series of OMC-tethered molecular catalysts, we demonstrate power densities ranging from 100 to 400 μW/mg Pt (Table 1), as opposed to previous technology that showed very low, unsteady open circuit voltage (OCV) at less than 105 mV and produced no measurable current from the fuel cell.[8] Additionally, this work demonstrates substantial improvement in power density over the initial publication from the General Electric Corporation demonstrating 2.2 μW/mg Pt.[7]

The polarization curves and the power density performance for all six OMC-bound molecular catalysts, measured using optimized fuel cell conditions, are shown in Figure 3B−E. All OMC-tethered single-site catalysts gave substantially higher OCV than previous DMEFC studies. Specifically, OMC-4Bp-Pt-Cl_2 reached a voltage as high as 0.53 V, whereas its control, OMC-4Bp, which has no platinum complex bound on the surface, had an OCV of 0 V (Figure S7). Also, controls using Vulcan as the carbon

Table 1. Power Densities Obtained from the Series of OMC-Tethered Molecular Catalysts As Compared to Previously Reported and Commercially Available Catalysts in a DMEFC

entry	sample	power (μW/mg Pt)
1	OMC-6Bp-Pt-Ph_2	83
2	OMC-6Bp-Pt-Ph_2 + 20% OMC	122
3	OMC-4Bp-Pt-Ph_2	101
4	OMC-phen-Pt-Ph_2	103
5	OMC-6Bp-Pt-Cl_2	127
6	OMC-4Bp-Pt-Cl_2	278
7	OMC-4Bp-Pt-Cl_2 + 20% OMC	403
8	OMC-phen-Pt-Cl_2	109
9	Commercial GDE Pt/C	87
10	General Electric (Niedrach, 1962) Pt	2

support for one of the molecular catalysts demonstrated negligible activity (Figure S8). At open circuit, chemical reactions at the electrodes are in equilibrium and the OCV directly measures the difference in the chemical activity of methane at the anode and the cathode. Although it took approximately 30 min to reach the equilibrium state, the improved OCV indicates superior performance of the OMC-supported molecular catalysts in DMEFC compared to the previous catalysts.[7,8] The convex-down curvature of the polarization curves is attributed to methane crossover that is oxidized minimally by the reduced Pt on the cathode, as is expected by previously published work on methane oxidation catalyzed by Pt metal.[7,8]

In general, the chlorine variants of the molecular complexes gave higher current and power densities than their phenyl counterparts possibly due to the difference in the mechanism of C−H activation. Although we have no direct evidence, the Pt−Cl catalysts might access cationic Pt/chloride ion pairs. Related ion pairs have been suggested to be involved in Pt(II) mediated methane activation using different catalysts.[31,42,43] Accessing such species is less likely from the corresponding Pt−Ph species. OMC-4Bp-Pt-Cl_2 showed the greatest activity in methane fuel cells at approximately 80 μA cm^{-2} at 0.2 V with a maximum power density of 278 μW/mg Pt. These values are significantly higher than previously reported values (Table 1, entry 10).

Higher power densities were observed when 20% unfunctionalized OMC was mixed with the molecular catalyst tethered OMC, possibly due to the higher conductivity of the unfunctionalized OMC support. The results showed a significant improvement in both the current and the power density, which were nearly 50% higher than those of the catalyst alone for both the lowest (OMC-6Bp-Pt-Ph_2) (Table 1, entries 1 and 2) and the highest (OMC-4Bp-Pt-Cl_2) (Table 1, entries 6 and 7) performing catalysts. A maximum normalized power of 403 μW/mg Pt was obtained, which was 5 times higher than that for a modern commercial catalyst and 2 orders of magnitude greater than that for Pt black catalyst (Table 1, entry 7). To our knowledge, this is the highest power output (μW/mg Pt) obtained from a direct methane fuel cell operating at low temperatures (80 °C).

Interestingly, the polarization curves measured for OMC-phen-Pt-Cl_2 did not follow the pattern typically observed in PEMFC, where high current densities are observed (see Figure 4A for OMC-phen-Pt-Cl_2). In PEMFC, the polarization appears with a logarithmic drop at the initial decrease in voltage, which is referred to as the activation region, followed by a linear region due to the ohmic resistance of the cell. At low voltage, the mass transfer region appears where the current reaches a limiting value because the transport hindrances limit the supply of fuel to the active sites. In this methane system, the voltage quickly dropped to zero after a finite load resistance allowed electrons to go through the external circuit. Since the steep decreasing voltage occurred at very low current density, it could be associated with mass transport limitation and slow sorption kinetics of methane at the anode.[7] Several of the lower performing polarization curves in Figure 3B appear to reach the linear ohmic region at 0.1 V, indicating that the poor kinetics of methane oxidation still dominate the system.

To further elucidate the limiting performance of the fuel cell, we investigated both the utilization of methane and the kinetics of methane oxidation. With the use of the Randles-Sevcik equation, the diffusion coefficient of methane (shown in Figure 4B) was estimated at 3.19×10^{-12} cm^2 s^{-1} (see Supporting information for detailed explanation on the calculation). The Cottrell plot produced from our measurements approaches the origin as has been previously described.[44] This describes the two-phase boundary reaction zone where the methane permeates, dissolves into the electrolyte, and diffuses toward the electrode. For reference, the diffusion coefficient of hydrogen at the anode in hydrogen PEM fuel cell is only about 10^{-2} cm^2 s^{-1},[45] which indicates a major limitation to be overcome is the transport of methane to reach the reactive sites. As previously mentioned, another challenge in this system is the slow sorption kinetics. Since adsorption of methane is an initial step before the reaction occurs and desorption is the final step to remove the products, slow sorption would delay the reaction and lower the cell performance. To separate the effects of anode electrode reaction kinetics from mass transport, anodic polarization was used to analyze the anodic half-cell. For this experiment, nitrogen was fed to the cathode (rather than oxgyen), which became a pseudoreference electrode, and a potentiostat was used to polarize the anode to force methane to oxidize. From the anode polarization, the Tafel slope was extracted (and its value could be related directly to the electrocatalytic activity).[46] The smaller the slope, the better the cell performance since higher current density is obtained at a given voltage.

From the inset on Figure 4C, which shows the data in a semilog format, the Tafel slope was extracted between 0.2 and 0.5 V, and the estimated slope was 592 mV dec^{-1}. At the same temperature and pressure conditions, using Pt catalyst, typical Tafel slopes for hydrogen and methanol are about 25 and 161 mV dec^{-1}, respectively.[47,48] The values of the Tafel slopes indicate that the activation energy required for methane oxidation at the fuel cell anode is almost 24 times higher than that for hydrogen oxidation and 4 times higher than that for methanol oxidation. This is not surprising considering the challenge in low temperature activation of methane; however, these results are the first demonstration that methane activation at these temperatures is possible.

After fuel cell testing, the catalyst was characterized with FT-IR to probe for the presence of Pt-carbonyl, as CO adsorption would have a negative impact on the performance of the catalyst. The absence of CO adsorption peaks at at 2186, 2087, and 1860 cm^{-1} in the FT-IR after methane oxidation indicated no catalyst poisoning by formation of Pt-CO units (Figure S7).[49−52] This coincides with data we obtained from measuring CO reactivity with the molecular catalyst (Figures S10 and S11). Finally, chronoamperometry was performed by holding the fuel cell at 0.2 V to generate current and allowing the effluent to pass through a CO_2 trap that contained 1 M NaOH solution to determine if CO_2 was produced over a 20 h period. ^{13}C NMR was used to characterize the bicarbonate solution collected in this

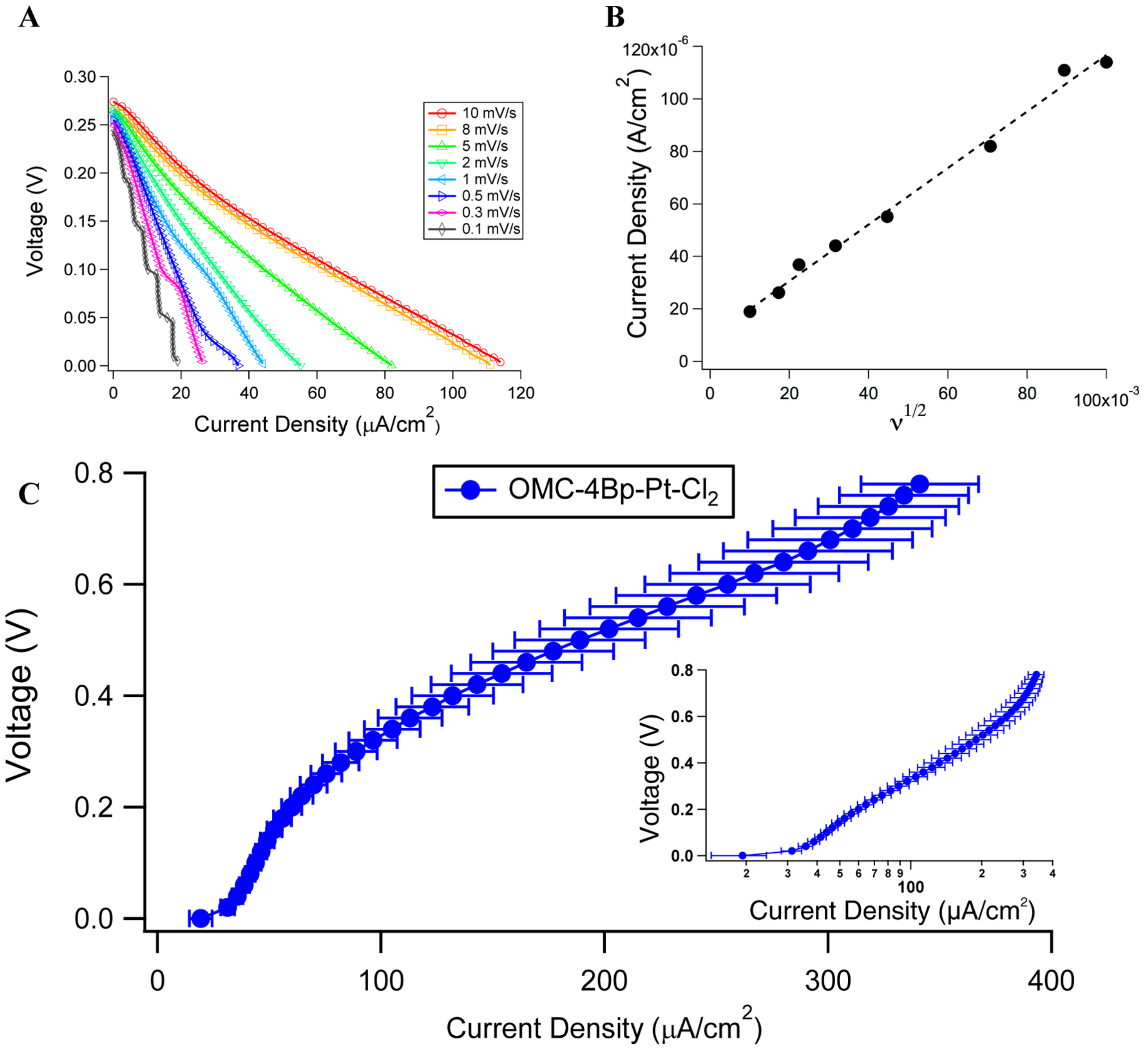

Figure 4. Studies of mass transport and reaction kinetics during methane oxidation at the anode. (A) Polarization curves at different scan rates of fuel cell with OMC-phen-Pt-Cl_2 on the anode and commercial GDE containing 0.5 mg Pt cm^{-2} on the cathode. (B) The corresponding Cottrell plot for the polarization curves with OMC-phen-Pt-Cl_2 measured at zero potential. (C) Anode polarization of OMC-4Bp-Pt-Cl_2 at 30 psig with Tafel plot in the inset.

trap. The spectra revealed the presence of CO_3^{2-} indicating that CO_2 was produced in the fuel cell effluent under these conditions (Figure S8). Also, no current density, and hence no bicarbonate formation, was observed in the absence of methane ruling out the possibility of OMC oxidation. The OMC bound ligands that were used as controls, OMC-4Bp, OMC-6Bp, and OMC-phen, that did not contain Pt as shown XPS spectra (see next section for details) showed negligible current densities in DMEFCs in the presence of methane and zero production of CO_2 by ^{13}NMR. Clearly, the observed carbonate was the product of methane oxidation to CO_2. The OMC-4Bp-Pt-Cl_2 catalyst sample was analyzed after the fuel cell reaction using electron microscopy (Figure 5). It was observed that the molecular Pt(II) complex decomposed to metallic Pt nanoparticles which led to the deactivation of the methane oxidation catalyst. High resolution STEM and EDX (Figure 5E−G) indicated the presence of crystalline Pt nanoparticles.

Chronopotentiometry was used to test the durability of the direct methane PEMFC at an applied current density of 19.3 mA cm^{-2} at 80 °C. As Figure S12 shows, the voltage was stable at 0.2 V for 6 h before it dropped to 0 V. After 10 h, the voltage became negative indicating a switch potential of the electrodes. It is most likely that the redox reactions continued to generate electrons at the anode that migrated to the cathode through the external circuit. However, the transport of the protons, produced from methane oxidation at the interface between the anode and the membrane, was hindered due to currently available ionomer polymer technology under anhydrous conditions (see Supporting Information for details on hydration effect). Experiments were completed at various humidity levels and optimized conditions were used for all reported experiments (see Supporting Information for optimization studies). As a result, charges built up at the anode and cathode generating a negative potential. Also, CV was measured on one sample that demonstrated current production and no redox peak for Pt was observed (Figure S9).

Insights Using X-ray Photoelectron Spectroscopy (XPS). It was observed that most of the activity values obtained from the electrochemical measurements for each OMC-tethered catalyst correlate directly with the observations recorded from the XPS studies. Considerable insights regarding the relationship between the structure, composition and activity can be gained

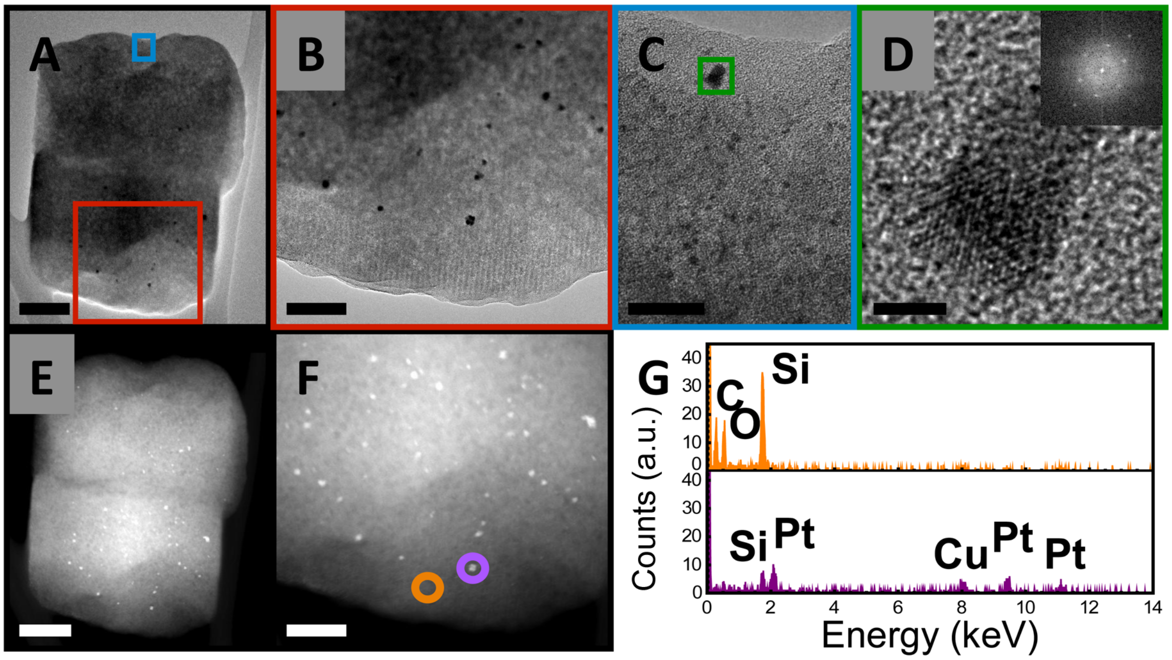

Figure 5. Bright field and scanning transmission electron micrographs of the catalyst OMC-4Bp-Pt-Cl_2 after fuel cell testing, showing high contrast Pt metal nanoparticles disbursed across the support material. (A) TEM image of the entire particle. Scale bar = 200 nm. (B) Higher magnification image of the particle edge, indicated by the red box in (A), showing the pore structure of the carbon support from the side, as well as a distribution of larger nanoparticles. Scale bar = 100 nm. (C) Higher magnification image of a thinner area of the particle edge, indicated by the blue box in (A), showing the presence of many smaller nanoparticles. Scale bar = 20 nm. (D) High resolution image of the medium-sized nanoparticle indicated by the green box in (C), with corresponding fast Fourier transform inset showing single crystalline structure. Scale bar = 2 nm. (E and F) STEM images corresponding to (A) and (B). Scale bars = 200 and 50 nm, respectively. (G) EDX spectra collected in the regions indicated by the colored circles in (F), corresponding to the OMC support (orange) and a single Pt nanoparticle (purple). The spectrum acquired in the purple circle is representative of spectra taken on numerous other particles in this region. Elemental analysis shows that the indicated particle and other particles consist of Pt, while the HRTEM (D) shows that the nanoparticles are single crystalline, and are thus reduced metal Pt.

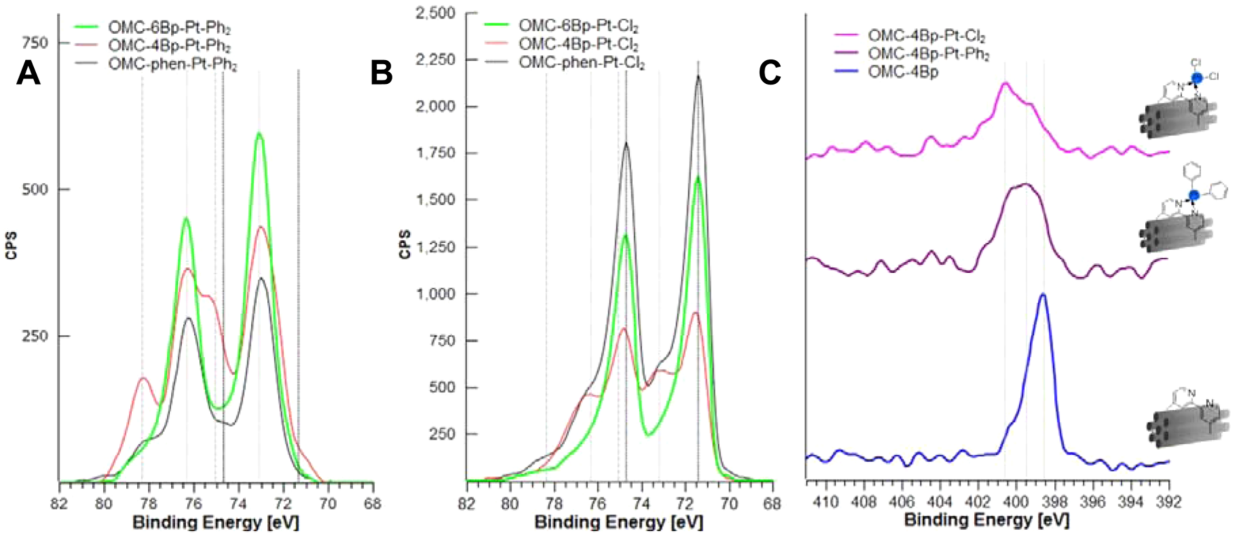

Figure 6. High-resolution XPS spectra. (A) Pt 4f, phenyl derivatives; and (B) Pt 4f, chloro derivatives of the complexes. (C) N 1s, comparing chloro, phenyl, and non-platinum versions. The peaks at 398.6 and 399.4 eV are due to uncoordinated bipyridine moieties; peak at 400.6 eV, clearly visible in the purple and pink spectra corresponding to Pt-containing chloro and phenyl versions, is attributed to the N−Pt coordination. The control made without platinum (blue) shows only negligible peak intensity at 400.6 eV.

through these measurements. As seen from Figure 6A, the high-resolution Pt 4f spectra of all three phenyl versions of the OMC supported single-site catalysts showed a predominant peak corresponding to the Pt $4f_{7/2}$ component positioned at 73.0 eV, indicating that Pt was in the +2 oxidation state. Another peak positioned at 75.0 eV was also observed in these spectra, which may be attributed to the excess Pt precursor ($[PtPh_2(\mu\text{-}SEt_2)]_2$) adsorbed onto the surface of OMC. Likewise, the high-resolution Pt 4f spectra obtained from three chloro derivatives of the OMC supported complexes revealed a major peak positioned at 71.4 eV (Figure 6B). This lower binding energy peak is distinctive to $PtCl_2$ moieties and has been attributed to a higher charge accumulation on the Pt in the $PtCl_2$ as compared to $PtPh_2$, maintaining Pt in the +2 oxidation state, which is also consistent with the notion that heterolytic Pt−Cl cleavage is a viable pathway for methane C−H activation (see above).[53]

Furthermore, it was evident from the XPS data that the activities of the OMC-based catalysts were dependent on several factors such as the quantity of bipyridine moieties coordinated to Pt(II), the atomic concentration of Pt and N and finally, the atomic concentration of Cl in the catalyst sample. In the deconvoluted high-resolution N 1s spectra of these catalyst samples (Figure 6C), two main peaks were observed. The peaks positioned at 398.6 and 399.4 eV were attributed to the uncoordinated bipyridine moieties on the surface of mesoporous carbon. The peak located at 400.6 eV was attributed to the N−Pt bonds, confirming the formation of the complex on OMC support.[54−56] These data, along with the atomic concentration of Pt and N, lend evidence for the role of molecular catalysts in the activation of methane in a PEM fuel cell. For example, the percent atomic concentrations of Pt and N in the samples OMC-4Bp-Pt-Cl_2 were 4 and 3.2, respectively (Table S2, entry 5). The highest catalytic activity in the DMEFC (278 μW/mg Pt) was observed when the major component of the N 1s peak was located at 400.6 eV, which was attributed to the coordinated nitrogen moieties (Figure 6C). On the contrary, in the phenyl version of this catalyst, OMC-4Bp-Pt-Ph_2, the percent atomic concentrations of Pt and N were observed to be 1.3 and 4.1 (Table S2, entry 2), respectively, implying a large excess of nitrogen compared to platinum. This was also reflected in the high-resolution N 1s spectra which, in addition to a peak at 400.6 eV due to coordinated species, also showed a substantial amount of uncoordinated species located at 398.8 and 399.4 eV (Figure 6C). Consequently, the electrocatalytic activity in the DMEFC was significantly lower (101 μW/mg Pt), presumably due to the small amount of complex on the surface of OMC. These results further validate the role of OMC-tethered molecular catalysts in the activation of methane in fuel cells.

Finally, it was observed that another contributing factor toward the activity in DMEFC was the quantity of Cl in the catalyst materials. For example, the OMC-4Bp-Pt-Cl_2 catalyst had the highest atomic concentration of Cl (Table S2, 1.7 at %) and demonstrated the highest catalytic activity (278 μW/mg Pt). Importantly, this sample also had the highest amount of nitrogen coordinated with Pt(II). The N/Pt ratio was 0.8 and was the highest among the chloro derivatives. In comparison, the OMC-phen-Pt-Cl_2 sample had significantly less Cl (Table S2, 0.9 at %) and a much smaller N/Pt ratio (0.4), which implies a lower quantity of phenanthroline coordinated Pt moieties. This material demonstrated lower activity (109 μW/mg Pt) than other catalysts in the OMC-Pt series. The sample showing the highest atomic concentration of platinum did not demonstrate the highest electrocatalytic activity (Table S2, OMC-phen-Pt-Cl_2, 5.1 atom %), nor did the sample containing the highest atomic concentration of nitrogen (OMC-4Bp-Pt-Ph_2, 4.1 atom %, most of it was in the uncoordinated state due to the low platinum atomic concentration), which underscores the importance of specific identity of the nitrogen-ligated platinum for the C−H activation of methane in the DMEFC. The OMC bound ligands that were used as controls, OMC-4Bp, OMC-6Bp, and OMC-phen, did not show the presence of Pt in their spectra and showed negligible current densities in DMEFCs. In general, XPS studies reveal that a near 1:1 ratio of Pt/N gave the highest power output. These data supports the fact that molecular catalysts are responsible for the methane oxidation as opposed to Pt nanoparticles.

CONCLUSIONS

The strategy of pairing molecular catalysts with OMC is a viable approach for low temperature electrochemical methane oxidation. Hence, molecular Pt catalysts, which have been shown to thermally activate C−H bonds for chemical transformations,[34−36] can be tethered to conductive OMC support to perform similar C−H activation in an electrochemical environment. Given this initial success, expanding the studies to new molecular catalysts tethered to OMC is promising; improving methane conversion from the conversion calculated from the optimized catalyst (8×10^{-3}) would be an initial starting point. Still, engineering and chemical challenges need to be addressed including the poor solubility of methane and sorption in the fuel cell along with enhancing the stability of the supported Pt catalysts. Additional studies are underway to improve GDE conductivity, optimize humidity levels, and identify more active catalysts.

ASSOCIATED CONTENT

Ⓢ Supporting Information

The Supporting Information is available free of charge on the ACS Publications website at DOI: 10.1021/jacs.5b06392.

Additional experimental procedures, materials characterization data and fuel cell optimization details (PDF)

AUTHOR INFORMATION

Corresponding Authors

*tbg7h@eservices.virginia.edu
*aherring@mines.edu
*btrewyn@mines.edu

Author Contributions

⊥M.J. and V.N. have contributed equally.

Notes

The authors declare no competing financial interest.

ACKNOWLEDGMENTS

All authors would like to acknowledge funding by the Center for Catalytic Hydrocarbon Functionalization, an Energy Frontier Research Center (EFRC) funded by the U.S. Department of Energy (DOE), Office of Science, Office of Basic Energy Sciences, under award DE-SC0001298. TSG acknowledged AES for support through an AES Graduate Fellowship in Energy Research. The authors acknowledge the use of instruments at the Electron Imaging Center for NanoMachines supported by NIH (1S10RR23057 to ZHZ) and CNSI at UCLA. The authors would like to thank BASF for the generous gift of the templating agent and 3M for the generous gift of the ionomer.

REFERENCES

(1) Kerr, R. A. *Science (Washington, DC, U. S.)* **2010**, *328*, 1624−1626.
(2) Lee, J.-J.; Myung, J.-H.; Ko, H. J.; Hyun, S.-H. *ECS Trans.* **2009**, *25*, 1143−1148.
(3) Murray, E. P.; Tsai, T.; Barnett, S. A. *Nature (London, U. K.)* **1999**, *400*, 649−651.
(4) Putna, E. S.; Stubenrauch, J.; Vohs, J. M.; Gorte, R. J. *Langmuir* **1995**, *11*, 4832−7.
(5) Wang, Z.; Weng, W.; Cheng, K.; Du, P.; Shen, G.; Han, G. *J. Power Sources* **2008**, *179*, 541−546.

(6) Shin, T. H.; Ida, S.; Ishihara, T. *J. Am. Chem. Soc.* **2011**, *133*, 19399−19407.

(7) Niedrach, L. W. *J. Electrochem. Soc.* **1962**, *109*, 1092−96.

(8) Ferrell, J. R., III; Sachdeva, S.; Strobel, T. A.; Gopalakrishan, G.; Koh, C. A.; Pez, G.; Cooper, A. C.; Herring, A. M. *J. Electrochem. Soc.* **2012**, *159*, B371−B377.

(9) Arndtsen, B. A.; Bergman, R. G. *Science (Washington, DC, U. S.)* **1995**, *270*, 1970−3.

(10) Holtcamp, M. W.; Labinger, J. A.; Bercaw, J. E. *J. Am. Chem. Soc.* **1997**, *119*, 848−849.

(11) Jones, W. D.; Feher, F. J. *Acc. Chem. Res.* **1989**, *22*, 91−100.

(12) Labinger, J. A. *J. Mol. Catal. A: Chem.* **2004**, *220*, 27−35.

(13) Lersch, M.; Tilset, M. *Chem. Rev. (Washington, DC, U. S.)* **2005**, *105*, 2471−2526.

(14) Periana, R. A.; Taube, D. J.; Gamble, S.; Taube, H.; Satoh, T.; Fujii, H. *Science (Washington, DC, U. S.)* **1998**, *280*, 560−564.

(15) Shilov, A. E.; S, G. B. *Russ. Chem. Rev.* **1987**, *56*, 442−464.

(16) Bar-Nahum, I.; Khenkin, A. M.; Neumann, R. *J. Am. Chem. Soc.* **2004**, *126*, 10236−10237.

(17) Groothaert, M. H.; Smeets, P. J.; Sels, B. F.; Jacobs, P. A.; Schoonheydt, R. A. *J. Am. Chem. Soc.* **2005**, *127*, 1394−1395.

(18) Labinger, J. A.; Herring, A. M.; Bercaw, J. E. *J. Am. Chem. Soc.* **1990**, *112*, 5628−5629.

(19) Joglekar, M.; Pylypenko, S.; Otting, M. M.; Valenstein, J. S.; Trewyn, B. G. *Chem. Mater.* **2014**, *26*, 2873−2882.

(20) Brushett, F. R.; Thorum, M. S.; Lioutas, N. S.; Naughton, M. S.; Tornow, C.; Jhong, H.-R.; Gewirth, A. A.; Kenis, P. J. A. *J. Am. Chem. Soc.* **2010**, *132*, 12185−12187.

(21) Ward, A. L.; Elbaz, L.; Kerr, J. B.; Arnold, J. *Inorg. Chem.* **2012**, *51*, 4694−4706.

(22) Annen, S. P.; Bambagioni, V.; Bevilacqua, M.; Filippi, J.; Marchionni, A.; Oberhauser, W.; Schonberg, H.; Vizza, F.; Bianchini, C.; Gritzmacher, H. *Angew. Chem., Int. Ed.* **2010**, *49*, 7229−7233.

(23) Bevilacqua, M.; Bianchini, C.; Marchionni, A.; Filippi, J.; Lavacchi, A.; Miller, H.; Oberhauser, W.; Vizza, F.; Granozzi, G.; Artiglia, L.; Annen, S. P.; Krumeich, F.; Gruetzmacher, H. *Energy Environ. Sci.* **2012**, *5*, 8608−8620.

(24) Valenstein, J. S.; Kandel, K.; Melcher, F.; Slowing, I. I.; Lin, V. S. Y.; Trewyn, B. G. *ACS Appl. Mater. Interfaces* **2012**, *4*, 1003−1009.

(25) Monro, S.; Scott, J.; Chouai, A.; Lincoln, R.; Zong, R.; Thummel, R. P.; McFarland, S. A. *Inorg. Chem.* **2010**, *49*, 2889−2900.

(26) Steele, B. R.; Vrieze, K. *Transition Met. Chem. (Dordrecht, Neth.)* **1977**, *2*, 140−4.

(27) Hodges, K. D.; Rund, J. V. *Inorg. Chem.* **1975**, *14*, 525−8.

(28) Giffin, G. A.; Haugen, G. M.; Hamrock, S. J.; Di Noto, V. *J. Am. Chem. Soc.* **2013**, *135*, 822−834.

(29) Ferrell, J. R.; Kuo, M. C.; Herring, A. M. *J. Power Sources* **2010**, *195*, 39−45.

(30) Sanchez-Gonzalez, J.; Macias-Garcia, A.; Alexandre-Franco, M. F.; Gomez-Serrano, V. *Carbon* **2005**, *43*, 741−747.

(31) Shilov, A. E.; Shul'pin, G. B. *Chem. Rev. (Washington, DC, U. S.)* **1997**, *97*, 2879−2932.

(32) Johansson, L.; Ryan, O. B.; Tilset, M. *J. Am. Chem. Soc.* **1999**, *121*, 1974−1975.

(33) Johansson, L.; Tilset, M.; Labinger, J. A.; Bercaw, J. E. *J. Am. Chem. Soc.* **2000**, *122*, 10846−10855.

(34) McKeown, B. A.; Gonzalez, H. E.; Friedfeld, M. R.; Gunnoe, T. B.; Cundari, T. R.; Sabat, M. *J. Am. Chem. Soc.* **2011**, *133*, 19131−19152.

(35) McKeown, B. A.; Gonzalez, H. E.; Gunnoe, T. B.; Cundari, T. R.; Sabat, M. *ACS Catal.* **2013**, *3*, 1165−1171.

(36) McKeown, B. A.; Prince, B. M.; Ramiro, Z.; Gunnoe, T. B.; Cundari, T. R. *ACS Catal.* **2014**, *4*, 1607−1615.

(37) Ji, X.; Lee, K. T.; Holden, R.; Zhang, L.; Zhang, J.; Botton, G. A.; Couillard, M.; Nazar, L. F. *Nat. Chem.* **2010**, *2*, 286−293.

(38) Joo, S. H.; Choi, S. J.; Oh, I.; Kwak, J.; Liu, Z.; Terasaki, O.; Ryoo, R. *Nature (London, U. K.)* **2001**, *414*, 470.

(39) Nam, J.-H.; Jang, Y.-Y.; Kwon, Y.-U.; Nam, J.-D. *Electrochem. Commun.* **2004**, *6*, 737−741.

(40) Tessonnier, J. P.; Villa, A.; Majoulet, O.; Su, D. S.; Schlogl, R. *Angew. Chem., Int. Ed.* **2009**, *48*, 6543−6546.

(41) Kruk, M.; Jaroniec, M. *Chem. Mater.* **2001**, *13*, 3169−3183.

(42) Zhu, H. J.; Ziegler, T. *J. Organomet. Chem.* **2006**, *691*, 4486−4497.

(43) Kua, J.; Xu, X.; Periana, R. A.; Goddard, W. A. *Organometallics* **2002**, *21*, 511−525.

(44) Kamat, A.; Huth, A.; Klein, O.; Scholl, S. *Fuel Cells* **2010**, *10*, 983−992.

(45) O'Hayre, R., Cha, S., Colella, W., Prinz, F. *Fuel Cell Fundamentals*; John Wiley & Sons, Inc.: Hoboken, NJ, 2006; pp 137−168.

(46) Cooper, K. R.; Ramani, V.; Fenton, J. M.; Kunz, H. R. *Experimental Methods and Data Analyses for Polymer Electrolyte Fuel Cells*, 1.2 ed.; Scribner Associates, Inc.: Southern Pines, NC, 2005.

(47) Ferrell, J. R.; Kuo, M. C.; Turner, J. A.; Herring, A. M. *Electrochim. Acta* **2008**, *53*, 4927−4933.

(48) Song, C. J.; Tang, Y. H.; Zhang, J. L.; Zhang, J. J.; Wang, H. J.; Shen, J.; McDermid, S.; Li, J.; Kozak, P. *Electrochim. Acta* **2007**, *52*, 2552−2561.

(49) Benvenutti, E. V.; Franken, L.; Moro, C. C.; Davanzo, C. U. *Langmuir* **1999**, *15*, 8140−8146.

(50) Hill, G. S.; Rendina, L. M.; Puddephatt, R. J. *J. Chem. Soc., Dalton Trans.* **1996**, 1809−1813.

(51) Yamamoto, T.; Shido, T.; Inagaki, S.; Fukushima, Y.; Ichikawa, M. *J. Phys. Chem. B* **1998**, *102*, 3866−3875.

(52) McKeown, B. A.; Foley, N. A.; Lee, J. P.; Gunnoe, T. B. *Organometallics* **2008**, *27*, 4031−4033.

(53) Aw, B. H.; Looh, K. K.; Chan, H. S. O.; Tan, K. L.; Hor, T. S. A. *J. Chem. Soc., Dalton Trans.* **1994**, 3177−82.

(54) Artyushkova, K.; Kiefer, B.; Halevi, B.; Knop-Gericke, A.; Schlogl, R.; Atanassov, P. *Chem. Commun. (Cambridge, U. K.)* **2013**, *49*, 2539−2541.

(55) Ferragina, C.; Massucci, M. A.; Mattogno, G. *J. Inclusion Phenom. Mol. Recognit. Chem.* **1989**, *7*, 529−36.

(56) Onoa, G. B.; Moreno, V.; Font-Bardia, M.; Solans, X.; Perez, J. M.; Alonso, C. *J. Inorg. Biochem.* **1999**, *75*, 205−212.

DOI: 10.1021/jacs.5b06392
J. Am. Chem. Soc. XXXX, XXX, XXX−XXX